DRAFT VERSION JUNE 12, 2008
Preprint typeset using LaTeX style emulateapj v. 6/22/04

RADIAL DISTRIBUTION OF X-RAY POINT SOURCES NEAR THE GALACTIC CENTER

JAESUB HONG[1*], MAUREEN VAN DEN BERG[1], JONATHAN E. GRINDLAY[1],
XAVIER KOENIG[1], SILAS LAYCOCK[2] AND PING ZHAO[1]

Draft version June 12, 2008

ABSTRACT

We present the log*N*-log*S* and spatial distributions of X-ray point sources in the Galactic Bulge (GB) fields. We compare the properties of 1170 X-ray point sources discovered from our deep (100 ksec) *Chandra* observations on three low extinction window fields near the Galactic Center (GC) with the X-ray sources in the other GB fields centered around Sgr B2, Sgr C, Arches Cluster and Sgr A* using *Chandra* archival data. To reduce the systematic errors induced by uncertain spectral types of the sources coupled with field-and-distance dependent extinction, we classify the X-ray sources using quantile analysis and estimate their flux accordingly. The result indicates the GB X-ray population is highly concentrated at the center, more heavily than the known models of the stellar distribution, and it extends out to $\gtrsim 1.5^\circ$ from the GC, following $1/\theta$ relation. Given a simple power law model for the X-ray spectra, the closer to the GC the intrinsically harder the X-ray spectra appear, but adding the 6.7 keV iron line emission in the model allows the spectra of the GB X-ray sources largely consistent across the region. This implies that the majority of these GB X-ray sources can be of the same or similar type. The observed X-ray source density is consistent with the majority being cataclysmic variables (CVs) and X-ray spectral properties support the idea that the most likely candidate among the known types is magnetic CVs, intermediate polars in particular, but the contribution of other types such as polars, while remaining uncertain, could be more substantial than considered in the past. The log*N*-log*S* distribution and the derived specific luminosity of the X-ray point sources in the GB fields cannot explain the Galactic Ridge X-ray emission, implying the presence of a truly diffuse component.

Subject headings: Galaxy: bulge — X-ray: binaries — X-ray: population

1. INTRODUCTION

The *Chandra* X-ray Observatory has opened a new era in studies of the X-ray sources in the GB. A series of shallow and deep *Chandra* observations in the GC region have revealed $\sim$ 1000 X-ray point sources over $2^\circ \times 0.8^\circ$ (Wang et al. 2002) and 2357 X-ray point sources over $16' \times 16'$ around the Sgr A* (Muno et al. 2003; hereafter M03). The X-ray luminosity and relatively hard spectra ruled out the majority of the GB X-ray point sources being normal stars, active binaries, young stellar objects, or quiescent low mass X-ray binaries (qLMXBs) (M03). From lack of real matches between the infrared (IR, $K < 15$) and X-ray sources in the Sgr A* field, Laycock et al. (2005) (hereafter L05) concluded that high mass X-ray binaries (HMXBs) cannot be more than 10% of the GB X-ray sources. While the leading candidate that fits the properties of these X-ray sources is now magnetic cataclysmic variables (CVs) (L05, Muno et al. 2004), the recent discovery of qLMXBs and millisecond pulsars with hard spectra in globular clusters implies qLMXBs, often misrecognized as CVs, could be more common in the GB than thought in the past (Wijnands et al. 2005; Bogdanov et al. 2005). Infrared (IR) searches for the counterparts of these GB X-ray sources have been actively pursued, but the exact nature of the sources is still elusive due to high obscuration by dust and source confusion by high star density.

We have conducted a series of deep (100 ksec) *Chandra* observations on three low extinction window fields – Baade's window (BW), Stanek's window (SW; Stanek 1998) and "Limiting window" (LW) – near the GC. These window fields allow us to observe the GB X-ray population and their Galactic radial distribution without obscuration by dust. We have discovered 1170 X-ray point sources in these fields and compare their distributions with X-ray sources in the other GB fields. We present a new approach using quantile analysis to minimize the systematic errors in flux estimation. We compare the X-ray distribution with the known models of the stellar distribution and investigate their nature. This work is part of our *Chandra* Multi-wavelength Plane (ChaMPlane) Survey designed to identify the space density of the low-luminosity accretion sources in the Galaxy (Grindlay et al. 2005).

2. OBSERVATIONS AND DATA ANALYSIS

We performed *Chandra*/ACIS-I observations on BW on 2003 July 9 (Obs. ID 3780), on SW on 2004 February 14/15 (Obs. ID 4547 and 5303), and on LW on 2005 August 19/22 and October 25 (Obs. ID 5934, 6362 and 6365) respectively. Due to the technical constraints, the SW and LW observations were segmented into a few intervals, which were stacked for analysis. Table 1 summarizes the observational parameters and X-ray source statistics of the window and other GB fields analyzed in this paper. For the Sgr A* field, we have stacked 14 observations from the archive, totaling 750 ksec exposure, and for easy comparison with other GB fields, we also use the result from a 100 ksec observation (Obs. ID 3665).

We have analyzed the data as a part of the ChaMPlane survey. For consistent analysis, we have developed a series of X-ray processing tools, based on the version 3.4 of CIAO package (Hong et al. 2005; hereafter H05). After initial screening of the CXC level-2 data (e.g. cut by good time intervals using background fluctuation, $< 3\sigma$), we search X-ray point sources by a wavelet detection algorithm (*wavdetect*, Freeman et al. 2002) with a significant threshold of 10^{-6}. The *wavdetect* routine is performed on each observation and the

* Send requests to J. Hong at jaesub@head.cfa.harvard.edu
[1] Harvard-Smithsonian Center for Astrophysics, 60 Garden St., Cambridge, MA 02138
[2] Gemini Observatory, 670 N. A'ohoku Place, Hilo, HI 96720

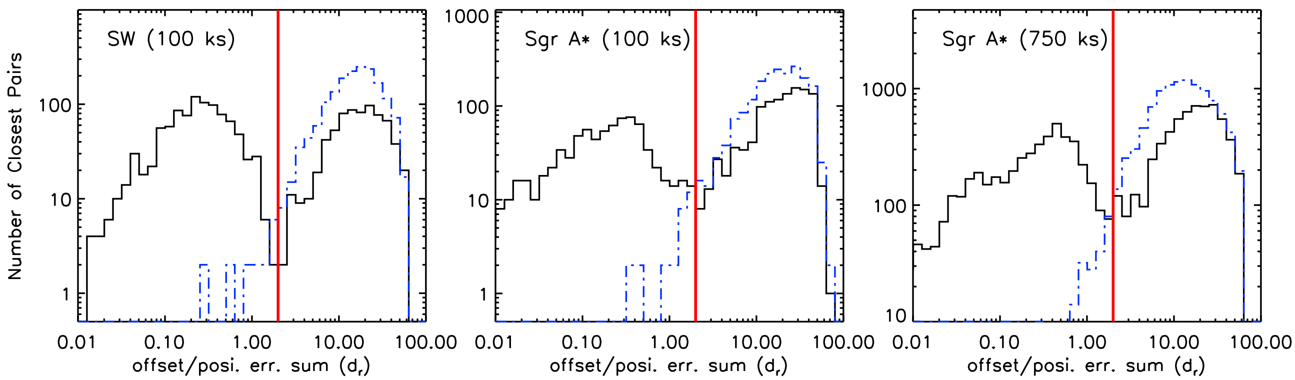

FIG. 1.— Cross correlating X-ray sources detected in three different bands: the number of pairs as a function of the relative offset (d_r) of the potentially identical sources (the closest pairs) among three bands. From left to right, the plot shows the results from the 100 ksec observation of the Stanek window, the Sgr A* field and 750 ksec of the Sgr A* field. The bimodal nature is due to the mixture of the true and random matches in the distribution. The (blue) dashed-dot line shows the results after introducing an arbitary global offset ($1.4'$ here) among three bands, which illustrates the distribution of the random matches.

stacked data set if available. Multiple observations are considered stackable (SW, LW and the Sgr A* field here) if their aimpoints are within $1'$ of each other's in the same instrument (ACIS-I or S).

In H05, we used source detections from broad (B_X: 0.3–8.0 keV) band. We now incorporate source detections from the soft (S_X: 0.3–2.5 keV) and hard (H_X: 2.5–8.0 keV) bands in addition to the broad band. We establish a unique source list (Table 1) by cross matching three detection lists based on the relative distance of possibly identical source pairs (the closest pairs) in three different bands. The relative distance (d_r) of two sources is defined by the ratio of the source distance to the quadratic sum of the positional errors. Note that there is no astrometric offset between three band images.

Establishing a unique source list is straightforward in relatively uncrowded or mildly dense fields such as windows fields, but it can be tricky in heavily populated fields such as the stacked observation of Sgr A*. Fig. 1 shows the distributions of the relative distances of two closest source pairs among three detection bands in 100 ksec observations of Stanek window and Sgr A* field and the 750 ksec stacked data set of Sgr A* field. A given source in each band contributes two pairs in the distribution, one from each of the other two bands.

The bimodal feature of the distribution indicates the two types of the pairs are mixed in the distribution: one for the truly identical sources detected in different bands and one for random pairs of unrelated sources. The distribution of the random pairs can be estimated by introducing an arbitrary global offset ($\sim 1.4'$ in Fig 1) in the source position between the detection bands, and the (blue) dash-dot line shows such an example, the shape of which mostly matches with the right side of the bimodal distribution with no offset.

After the visual inspection of the raw images and the distributions of the relative distances in Fig. 1, we use a simple cut ($d_r \leq 2.0$, red vertical line) for establishing the unique source list. The cut is sufficient for identifying virtually 100% of the identical sources detected in multiple bands. From the distributions of the relative distances of the random pairs from an arbitrary offset, we estimate that the false random matches by the cut ranges from 10 to 25 for $\sim$ 100 ksec observations. The corresponding expected number of missed independent sources by the false random matches ranges from 5 to 10 ($\sim$ 1%) and about 100 for stacked Sgr A* ($\sim$ 3%).

When multiple detections in the three bands are identified for a source, we select one with the smallest positional error for the unique source list. Note that the final source position and error could be derived from a form of weighted average of astrometric properties of multiple detection. Since the S_X and H_X band detections are not entirely independent from the B_X band detection, in order to avoid unnecessary complication in the analysis, we simply take the astrometric properties of the one with the smallest positional errors, which usually indicates the highest significance in detection among the three bands.

After source detection, we perform aperture photometry on each source to extract the basic source properties such as count, rate and quantiles in the conventional energy bands (S_C: 0.5–2.0, H_C: 2.0–8.0 and B_C: 0.5–8.0 keV). For the sources that fall near other sources, we carefully revise the aperture of the source regions to minimize the contamination from the neighbors (H05). Table 2 lists a part of the source catalog with source properties. The complete list for windows fields is available in the electronics edition.

3. FLUX ESTIMATION BY QUANTILE CLASSIFICATION

In order to compare source distribution in various regions of the sky with diverse extinctions, it is necessary to resolve the interstellar absorption and find the unabsorbed source flux, but such calculation is not trivial for X-rays sources with diverse spectral types found in Galactic plane fields. Faint sources are unsuitable for spectral fitting. The relatively large extinction in the GB fields and its usually-unknown field-and-distance dependent variation make it even harder to identify the spectral type. Inaccurate assumption of the spectral type in flux estimation introduces the dominant systematic errors that often exceed the statistical errors. To overcome this difficulty and measure the severity of the problem, we employ quantile analysis (Hong et al. 2004; hereafter H04). Ebisawa et al. (2005) employs a similar approach using hardness ratio, but due to the diverse spectral types and the large variation of the interstellar absorption seen in the GB fields, quantiles, free of count-dependent bias inherent in X-ray hardness ratio or X-ray color analysis, provide a better measure in classifying X-ray sources in the GB fields (H04).

3.1. *Quantile Analysis*

Fig. 2 shows the quantile diagrams of the X-ray sources ($S/N \geq 3$ in B_X) in the selected GB fields overlaid with grids

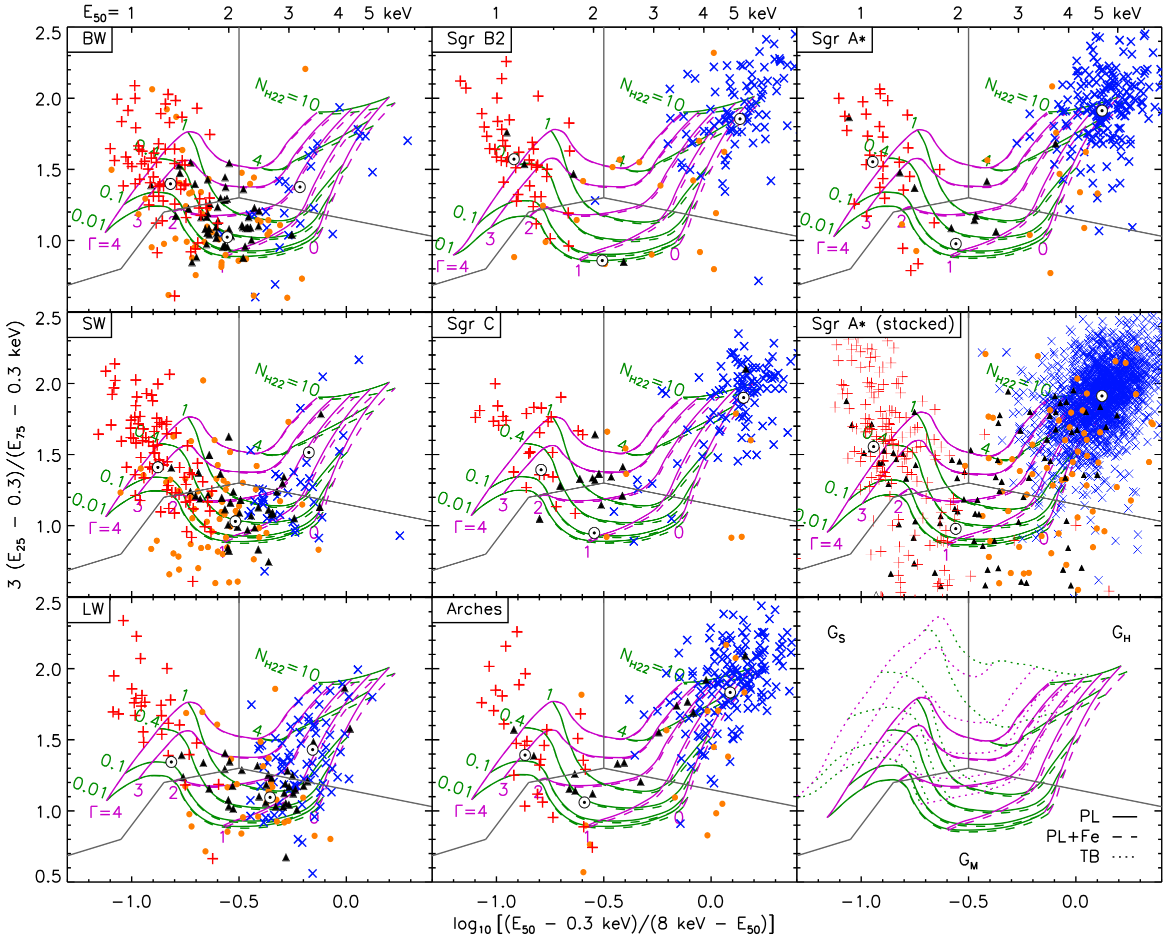

FIG. 2.— Quantile diagrams (0.3–8 keV) of the X-ray sources with $S/N \geq 3$ in the GB fields overlaid with grids for a simple power law model (PL, solid lines, $\Gamma = 0$, 1, 2, 3 & 4, $N_{\rm H22} = 0.01$, 0.1, 0.4, 1 & 10), a power law plus an iron line model (PL+Fe, dashed, at 6.7 keV with 0.4 keV EW), and thermal Bremsstrahlung model (TB, dotted, $kT = 0.2$, 0.4, 1, 2, 4 & 10 keV, $N_{\rm H22} = 0.01$, 0.1, 0.4, 1 & 10, only shown in the bottom-right plot for clarity). The energy quantile E_x corresponds to the energy below which x% of the counts are detected. The (red) crosses are for the relatively soft sources ($S/N \geq 3$ in S_C, but not in H_C), the (blue) 'x's for the hard sources ($S/N \geq 3$ in H_C, but not in S_C), the (black) triangles for the bright sources ($S/N \geq 3$ in both S_C and H_C), and the (orange) dots for the faint sources ($S/N \geq 3$ only in B_C). The (grey) lines from (–0.5,1.3) divide each diagram into the soft (G_S), medium (G_M) and hard groups (G_H). $\odot$ shows the quantiles of stacked photons in each group.

for a simple power law model (PL, solid lines), a power law plus an iron line emission (PL+Fe, dashed, see §3.2 for motivation) at 6.7 keV with 0.4 keV equivalent width (EW), and the thermal Bremsstrahlung model (TB, dotted). The S/N here is calculated based on the statistical errors (σ_s) using Gehrels et al. (1986) (see also H05). The difference in the model grids between PL and PL+Fe is only evident in the highly absorbed or very hard section of the diagram (right-top) because a small iron line (> 6 keV with < 1 keV EW) does not make a noticable difference in three quantiles of the soft sources.

Relatively insensitive to the extinction or the model class in comparison (PL, PL+Fe or TB), the sources around $(x, y) = (-0.9, 1.6)$, present in every field, appear unabsorbed and intrinsically soft. The foreground thermal sources such as coronally active stars fit the description. The location of relatively hard sources in the diagram varies with the field extinction. In the window fields, the hard sources are relatively unabsorbed, but on approach to the GC, there is an increasing trend in the source number with both the average absorption and the intrinsic hardness, when compared to a simple power law model. For instance, in BW most sources lie in power law photon index (Γ) > 1 and $N_{\rm H22} < 1$, whereas in LW many sources lie in $\Gamma < 1$ and $N_{\rm H22} > 1$. In the Sgr A* field and the rest, most of the hard sources are heavily absorbed with $\Gamma \lesssim 1$ on average, well separately from the foreground sources.

The quantile diagrams nicely illustrate the spectral diversity of the X-ray sources in the GB fields, but poor photon statistics also contributes to the scatter. To reduce systematic errors caused by poor statistics in assigning spectral types while allowing the spectral diversity of the sources in each field, we divide the diagram into three groups as shown by the (grey) lines originating at (–0.5, 1.3). The left panel represents the foreground thermal sources (G_S: soft group), the middle panel the unabsorbed accreting sources (G_M: medium group), and the right panel the absorbed thermal or accreting sources (G_H: hard group). The division between G_S and G_H is devised to be robust against variations in detector response: e.g. ACIS-I vs. ACIS-S (see H04; H05), temporal loss of low energy response. The final results (e.g. log$N$-log$S$) are not sensitive to small changes of the group division boundaries (e.g. shifting the boundaries by ~ 0.1 in x or y).

Under the given model class (e.g. PL), to estimate the spectral model parameters (e.g. Γ and $N_{\rm H}$) of the sources in each group, we use the quantiles (marked by $\odot$) of the stacked photons of the sources in the group that have $S/N \geq 3$ and net counts ≤ 1000 (not to be dominated by a few bright sources) in B_X.

TABLE 1
X-RAY POINT SOURCES IN THE SELECTED GB FIELDS

Field	l (°)	b (°)	[a]Off. (°)	[b]N_{H22}	[c]GTI (ks)	Source count[d] B_X	S_X	H_X	Combined
BW	1.06	–3.83	3.93	0.31	96	365	334	135	411
SW	0.25	–2.15	2.12	0.48	96	389	313	141	434
LW	0.10	–1.43	1.39	0.68	94	286	188	174	325
Srg B2	0.59	–0.03	0.65	81.2	97	281	129	225	367
Srg C	–0.57	–0.02	0.51	52.7	97	321	203	243	459
Arches	0.12	–0.02	0.19	52.5	97	331	87	334	431
Sgr A*	–0.06	–0.05	–	56.5	88	548	98	419	548
(Stacked[e])					698	2348	398	2486	2982

(a) The aim point offset from the GC. (b) The estimates by Schlegel et al. (1998) at the aim point for the sum along the line of the sight in 10^{22}cm^{-2}. (c) The good time intervals (GTIs). The total exposure is 100 ksec each (750 ksec for the stacked Sgr A* field). (d) The number of the sources from the ACIS-I CCDs (0, 1, 2, and 3) in the three detection bands (B_X: 0.3–8 keV, S_X: 0.3–2.5 keV, H_X: 2.5–8 keV) and the combined uniq list. (e) Obs. ID: 242, 2951 ... 2954, 2943, 3663, 3392, 3393, 3549, 4683, 4684 and 5360.

TABLE 2
CATALOG OF X-RAY POINT SOURCES IN THE WINDOW FIELDS

Source Name (CXOPS J)	Field	R.A. (°)	Dec. (°)	Posi. Error[a] (″)	Offset[b] (′)	Net counts S_C	H_C	Quantiles E_{50} (keV)	Quartile Ratio[c]	Unabsorbed Flux[d] S_C (10^{-14} erg s^{-1} cm^{-2})	H_C
80230.4-295647	BW	270.626934	-29.946497	1.29	10.05	71.5 (10.9)	53.3 (9.9)	1.89 (0.10)	1.30 (0.17)	1.00 (0.15)	1.31 (0.24)
80231.2-295528	BW	270.630007	-29.924698	2.37	10.12	4.6 (6.9)	34.8 (8.9)	3.56 (0.29)	1.68 (0.30)	0.38 (0.58)	1.12 (0.29)
80235.9-295323	BW	270.649946	-29.889846	3.32	9.87	23.4 (8.1)	-0.2 (5.6)	1.05 (0.15)	2.08 (0.48)	0.30 (0.10)	-0.01 (0.13)
....											
75404.4-294359	SW	268.518385	-29.733089	2.56	9.58	25.3 (9.2)	5.9 (6.6)	1.34 (0.18)	1.63 (0.64)	0.39 (0.14)	0.13 (0.14)
75405.3-294717	SW	268.522117	-29.788307	2.47	8.04	19.7 (7.7)	2.9 (5.1)	1.40 (0.24)	1.61 (0.40)	0.29 (0.11)	0.06 (0.11)
75406.7-294239	SW	268.527957	-29.711050	1.97	9.99	20.6 (9.4)	22.5 (8.0)	2.12 (0.54)	1.08 (0.32)	0.28 (0.13)	0.69 (0.24)
....											
75051.2-293418	LW	267.713518	-29.571797	1.02	8.10	36.2 (9.1)	75.8 (10.9)	2.63 (0.20)	1.25 (0.16)	0.71 (0.18)	2.21 (0.32)
75052.0-293319	LW	267.716827	-29.555400	2.92	8.14	5.2 (6.8)	9.3 (6.6)	0.97 (5.31)	0.20 (0.29)	0.10 (0.13)	0.27 (0.19)
75053.3-293207	LW	267.722097	-29.535548	2.12	8.29	2.8 (7.3)	22.4 (7.8)	3.46 (0.38)	1.74 (0.48)	0.17 (0.44)	0.77 (0.27)
....											

Notes.—This table shows a part of the complete list, which is available in the electronic edition.
(a) 95% error radius (b) offset from the aim point (c) $3(E_{25}-0.3)/(E_{75}-0.3$ keV). (d) Based on PL+FE using quantile analysis (see the text)

TABLE 3
SPECTRAL MODEL PARAMETERS FOR THE G_M AND G_H SOURCES

Field	E_{50} (keV)	Quartile Ratio[a]	PL from Quantile Diagram[b] Γ	N_{H22}	PL+Fe (He-α) from Quantile Diagram[c] Γ	N_{H22}	PL (+Fe He-α) from Spectral Model Fit[d] Γ	N_{H22}	EW[e]	χ_r^2
unabsorbed hard sources (G_M)										
BW	1.97(2)	1.02(1)	**1.38**(03)	0.31(03)	**1.42**(03)	0.32(05)	**1.36**(2)	0.26(01)	0.15	0.68
SW	2.10(5)	1.03(2)	**1.35**(07)	0.37(06)	**1.38**(10)	0.38(08)	**1.22**(3)	0.25(03)	–[f]	0.71
LW	2.66(4)	1.09(2)	**1.28**(07)	0.73(09)	**1.35**(07)	0.79(09)	**0.99**(2)	0.38(02)	–[f]	0.85
absorbed hard sources (G_H)										
BW	3.22(13)	1.38(9)	**1.66**(37)	2.20(70)	**1.74**(37)	2.30(70)	**1.22**(4)	1.66(16)	–[f]	0.89
SW	3.39(7)	1.52(4)	**1.77**(23)	2.90(50)	**1.91**(23)	3.10(50)	**1.58**(4)	2.78(19)	–[f]	1.61
LW	3.48(5)	1.43(3)	**1.21**(10)	1.95(15)	**1.32**(10)	2.10(20)	**1.30**(2)	1.88(06)	0.17	0.81
Sgr B2	4.75(4)	1.86(2)	**–0.37**(14)	3.40(80)	**0.25**(17)	5.70(90)	**0.50**(1)	6.20(22)	0.61	0.68
Sgr C	4.81(3)	1.90(2)	**–0.26**(10)	4.8(1.0)	**0.46**(21)	7.8(1.2)	**–0.10**(1)	3.95(18)	0.38	0.91
Arches	4.54(2)	1.83(1)	**0.14**(07)	4.00(50)	**0.67**(14)	5.70(70)	**0.85**(1)	5.17(12)	0.66	0.88
Sgr A*	4.69(2)	1.91(1)	**0.31**(14)	6.40(60)	**0.94**(14)	9.00(80)	**1.02**(1)	6.95(12)	0.46	0.89

(a) $3(E_{25}-0.3)/(E_{75}-0.3$ keV). (b) The parameter estimates by quantile diagram. (c) with a fixed 0.4 keV EW at 6.7 keV (d) By the spectral model fit. (e) the EW of 6.7 keV line. (f) No estimates due to poor statistics and the fit is done under PL. See §4.

3.2. *Spectral hardening on approach to GC?*

Table 3 summarizes the group quantiles and corresponding model parameters of the G_M and G_H sources under the PL and PL+Fe models. The table also shows the model parameters estimated from the spectral model fit on the stacked spectra, using power law plus a 6.7 keV line, where the EW of the line is derived through the free parameters of the width and relative normalization of the line. In order to increase photon statistics, we stacked the spectra of sources with net counts ≤ 1000 for spectral fitting. The 0.4 keV EW is chosen for the 6.7 keV line in the PL+Fe model for quantile analysis (and the log$N$-log$S$ distribution later) because it is roughly consistent with the EW estimated by spectral model fits on the G_H sources and Muno et al. (2004b) found the same for the bright sources in the Sgr A* field. Note that the 6.7 keV iron line emission has been also observed in the X-ray point sources in the shallow survey of the GC strip (Wang et al. 2002) and other part of the Galactic plane (Ebisawa et al. 2005). The 6.4 keV iron line is also present in some sources of the GB fields, but it is generally more prominent as unresolved diffuse emission (Wang et al. 2002). Our aperture photometry is designed to minimize possible contamination of the diffuse emission through background subtraction (H05).

Under the PL model, both groups show the increasing trend of hardness of the intrinsic spectra of the likely GB X-ray sources on approach to GC in latitude (i.e. $\Gamma \gtrsim 1$ for the window fields vs. $\Gamma < 1$ for other GB fields). This apparent trend can be attributed to a few factors. In the case of the G_M sources in the window fields, the group contains a large number of foreground coronal sources and background AGNs in addition to the GB sources. For instance, in the BW and SW, about 70% of the sources with $S/N \geq 3$ in the H_C band are background AGNs (see Fig. 5 in §5). Therefore, the trend might not be real.

The similar trend in the G_H group appears to be more realistic. However, comparing the PL+Fe model grid with the PL model grid in the quantile diagram hints this trend can be an artifact of using the PL model to some extent. Indeed the trend is alleviated under the PL+Fe model as shown in the model parameters estimated by both quantile diagram and the spectral fits (Table 3). Poor statistics in the G_H sources of BW and SW does not allow any meaningful constraint of the iron line emission in the spectra, but the stacked spectra of the G_H sources in the LW does show a clear hint of the 6.7 keV line (Fig. 3). The relatively weak line feature (EW ~ 0.17 keV) in the LW can be explained by the relatively large contribution of AGNs in the group compared to other GB fields (see Fig. 5 in §5).

With the inclusion of a 6.7 keV line, the power law index (Γ) is largely consistent across the GB fields with a possible exception of the Sgr C field. The result indicates that the galactic X-ray sources in the LW field may be the same type of sources seen in the other GB fields closer to the GC and thus the GB X-ray sources indeed extend out to at least 1.5° from the GC. The detail spectral analysis of the combined point sources vs. the diffuse emission will be presented elsewhere (Hong et al. 2008).

3.3. *Flux Estimates*

Based on the group model parameters, we estimate the source flux in the conventional energy bands, using the instrument response files at the aim point and scaling them for source position in the sky by the exposure map (H05)[2]. For the stacked data, we use the average response files weighted by the exposure of each observation.

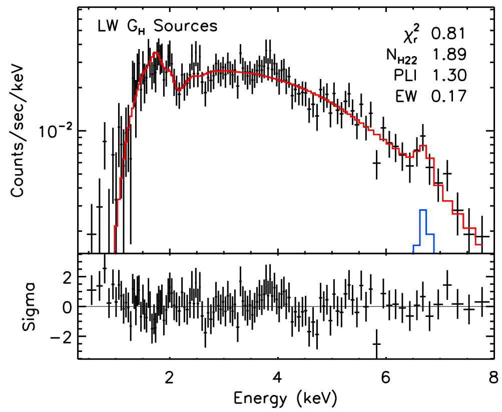

FIG. 3.— The stacked spectra of the G_H sources (net counts < 1000) in LW with the PL+FE XXV He-α (6.7 keV line) fit.

The quantile diagram can assign the proper model parameters (e.g. Γ=1.7 vs. 1.0) for the sources under a given model class, but it cannot determine which model class (e.g. PL vs. TB) is right for the sources. In order to estimate the systematic errors arising from the improper choice of the model class, we compare flux estimates under three different model classes: PL, PL+Fe and TB. In order to see the significance of the difference among these models, Fig. 4 compares count rate to unabsorbed flux conversion factor for each group and the three model classes for sources near the aim point. In the case of the H_C band the difference between the model classes is very small, but in the S_C band, the conversion factor can differ by more than a factor of 10. We also take the largest difference in the flux estimates among three models as the systematic errors (σ_c) and compare them with the pure statistical errors (σ_s). For the flux estimates in the H_C band, $\sigma_c \sim 20-30\%$ and we get $\sigma_c < \sigma_s$ for $\sim 87\%$ of the sources with $S/N \geq 3$, and $\sigma_c < \sigma_s$ for $\sim 62\%$ even with $S/N \geq 5$. In the S_C band, σ_c can be larger than 1000%, we get $\sigma_c < \sigma_s$ only for 28% with $S/N \geq 3$ and for 16% with $S/N \geq 5$.

This exercise does not explore all the possible model classes, but the results indicate the H_C band flux estimates in this method are robust and insensitive to the choice of the model classes. However, the S_C band flux estimates can be dominated by the systematic errors arising from improper selection of the spectral model. The fundamental difference between the S_C and H_C band here is that the S_C band is very sensitive to the range of interstellar absorption in the GB fields, $\sim 10^{21-23}$ cm^{-2}, while the H_C band is not. If the stacked photon counts of sources in a group are large enough, the spectral fit would be better suited for determining spectral type and parameters, although the spectral fit also often leave possible multiple choices. In the following, we limit our discussion to the H_C band results using the sources with $S/N \geq 3$ in H_C ('x's and triangles in Fig. 2), which are likely to be the GB sources (and AGNs) rather than the foreground sources.

4. SOURCE DISTRIBUTION

4.1. *Eddington and Malmquist Bias*

[2] The latest CIAO tools (ver 3.4 or higher) can calculate the response files appropriate to each source location

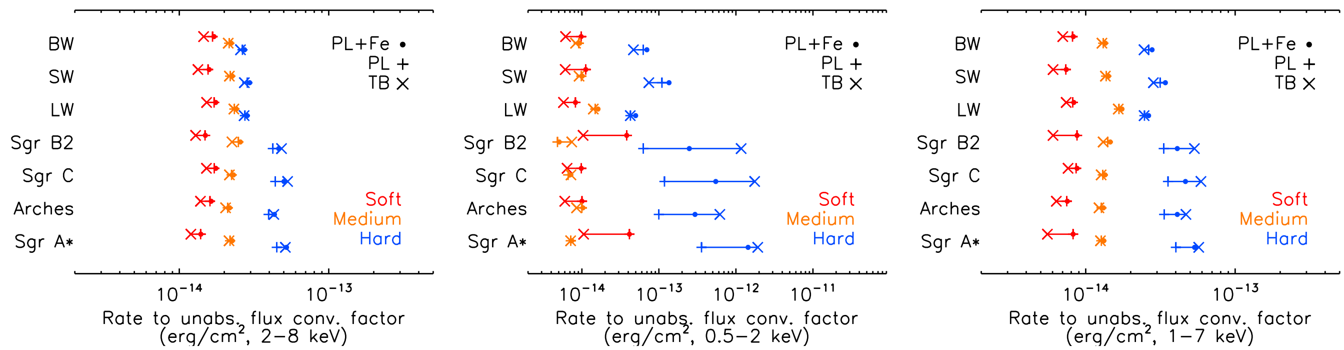

FIG. 4.— Comparison of rate-to-flux conversion factor for three groups of sources in the three energy range. The conversion factor in the H_C band (2–8 keV) is robust ($\lesssim$ 30–40%), in the S_C band (0.5–2 keV), it is very unreliable (up to more than a factor of 10), and in the medium energy range (1–7 keV), there are significant variations (up to $\sim$ 100%).

In order to explore the effect of the Eddington bias (EB) which makes the faintest sources appear brighter than they are, we simulate three spectral types of sources (one for each group) based on the group quantiles for each field. Using MARX[3], we generate the sources with a S^{-1} distribution and net counts (B_X) from 5 to 400. We scatter 200 – 250 of these sources randomly over the real events and apply the regular analysis procedure. We repeat the procedure 1000 times. The fake sources are not allowed to overlap each other but they can fall on top of the real sources. The results indicate that EB is noticable in the sources with <10 counts, which can appear as many as 15 – 20 count sources, depending on the field (or up to $\sim$ 30 count sources for the stacked Sgr A* field). Since we consider sources with $S/N \geq 3$ in the H_C band, which corresponds $\sim$ 16 – 20 counts at least ($\sim$ 30 counts for the stacked Sgr A* field), we expect EB is not a major contributor to the errors of the following distributions.

The Malmquist bias (MB) is due to the exposure dependent volume (depth) coverage. The MB is usually a concern for luminosity distributions but not for log$N$-log$S$ distributions in the apparent (detected) flux space. However, log$N$-log$S$ distributions in the unabsorbed flux space can have the MB when strong interstellar absorption limits the depth of the view, underestimating the true distribution. Therefore, the faint end of the log$N$-log$S$ distribution can be lower than the true distribution and so the MB counteracts the EB to some extent.

With ≥ 100 ksec exposure under the total of $N_{\rm H} = 12 \times 10^{22}$ cm^{-2}, all the sources with an unabsorbed flux of $\gtrsim 10^{-14}$ erg s^{-1} cm^{-2} can be seen at the far side of the Galaxy with $S/N \geq 3$ in H_C. Therefore the MB is not a concern above $\sim 10^{-14}$ erg s^{-1} cm^{-2} (or 5×10^{-15} erg s^{-1} cm^{-2} for the windows fields) for sources with a power law spectrum and Γ=1.0. Note this does not mean we can access X-ray sources of a certain luminosity all the way through the galaxy. For instance, the unabsorbed flux of $S > 10^{-14}$ erg s^{-1} cm^{-2} corresponds $L_X \gtrsim 8 \times 10^{31}$ erg s^{-1} at the GC (8 kpc) and $L_X \gtrsim 5 \times 10^{32}$ erg s^{-1} at 20 kpc, but considering the additional interstellar absorption between the GC and the far side of the Galaxy ($\sim 6 \times 10^{22}$ cm^{-2}), at 20 kpc, this is equivalent to $L_X \gtrsim 7 \times 10^{32}$ erg s^{-1} for a power law with Γ=1.0 if the unabsorbed flux was corrected only for the interstellar absorption out to the GC.

4.2. *Sky Coverage*

For the log$N$-log$S$ distribution, we need to know the sky coverage for the given flux value of each source. In order to avoid the systematic errors associated with spectral type assignment, we calculate the sky coverage of each source based on the detected photon counts of the three energy bands (Cappelluti et al. 2005; H05). For each observation, we generate the background-only images by removing the counts in the source regions in the image and filling the region with the counts using the statistics in the surrounding regions (*dmfilth*)[4]. At every sky point of the background images, we calculate the minimal detectable source counts ($S/N \geq 3$). For a given source, we take the sky area where the minimal counts are less than the net counts of the source in the band for the sky coverage. These sky coverage values agree well with the same expected from the simulated sources of three spectral types on average within 10% for the cases with $S/N > 3$. which indicates this method accounts for the completeness as well.

4.3. *The logN-logS and Radial Distribution*

Fig. 5 shows the log$N$-log$S$ and radial distributions of the X-ray sources in the GB fields, based on the flux estimates in the H_C band using the PL+Fe model. The log$N$-log$S$ distribution under the PL model (not shown in the left panel) is slightly lower than the same under the PL+Fe model in the high extinction fields and two distributions are nearly identical in the three low extinction window fields.

For the Sgr A* field, we plot the results from both the stacked data (black) and the 100 ksec exposure (grey). The spectral models from the 100 ksec exposure are used for the both data set. The distribution of the stacked data is $\sim$ 40% higher at $S > 10^{-14}$ erg s^{-1} cm^{-2} than the same of the 100 ksec exposure. A few factors such as the MB are responsible for the difference, but the main cause of the difference is suspected to be the X-ray variability of the sources. The stacked data (750 ksec) simply have a better chance of detecting them or catching them in a high flux state than the shorter exposure (100 ksec). For instance, the 20 brightest sources in the H_C band in the 100 ksec observation of the Sgr A* field are found to be about 30% brighter on average in the stacked data set, and five of the 20 brightest sources in the stacked data were not detected in the 100 ksec observation. This variation qualitatively agrees with the change seen in the log$N$-log$S$ distribution, but the diverse nature of the X-ray variability and duty cycles makes it hard to quantify the resulting difference in the log$N$-log$S$ distribution.

The overall normalization of the log$N$-log$S$ distributions in

[3] http://space.mit.edu/CXC/MARX/.

[4] http://cxc.harvard.edu/ciao/ahelp/dmfilth.html

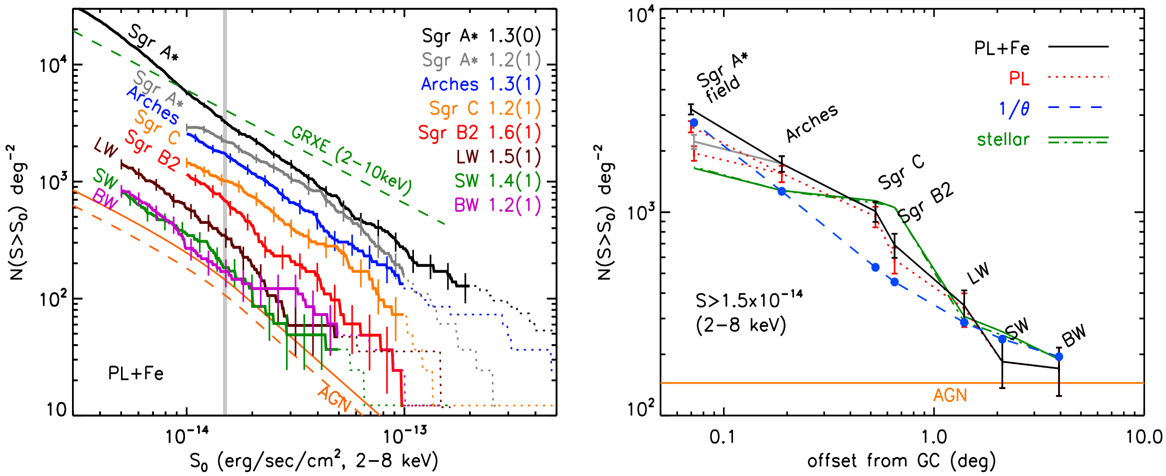

FIG. 5.— The log$N$-log$S$ (left) and the radial (right) distribution of the X-ray sources in the GB fields. Fluxes are computed for the sources with $S/N \geq 3$ in the H_C (2–8 keV) band, using the PL+Fe (0.4 keV EW at 6.7 keV line) model. The numbers indicate the slope (α) of the power law fits ($N \propto S^{-\alpha}$) to the log$N$-log$S$ distributions (solid lines). The active galactic nuclei (AGN) distribution is from Kim et al. (2007). The radial distribution shows the number density of sources at $S > 1.5 \times 10^{-14}$ erg s^{-1} cm^{-2} (marked by the vertical strip in the left panel) under two spectral models (solid black for PL+Fe and dotted red for PL), compared with the stellar models (solid green for 6-10 kpc and dashed dot green for 6-8 kpc) and the $1/\theta$ distribution (blue). The x-axis in the radiation distribution is the average offset values of the sources.

the GB fields are inversely proportional to the offset from the GC, however the slopes of the log$N$-log$S$ distributions are largely consistent with each other and 1.5, which is expected from the narrow FoV. The slope of the log$N$-log$S$ distribution is calculated by a straight line fit to the distribution and the y-axis error of the distribution is given by the quadratic sum of the statistical error (shown in the figure) and a constant systematic error ($\sim$ 40% from a conversative assumption of slope being -1.5) derived by $\sim$ 25% spectral model dependent error in the flux estimation. The AGN distribution is given from Kim et al. (2007), using a powerlaw model with Γ = 1.7 for the X-ray spectra. The dashed line indicates the reduced AGN population that can be seen through the high extinction fields such as Sgr A* field, since we correct the average absorption of the X-ray sources, $\sim 6 \times 10^{22}$ cm^{-2}, which is about the half of the total absorption for the AGN. For comparison, we overlay the necessary point source distribution to explain for Galactic Ridge X-ray emission (GRXE) at $(l, b) \sim (28.5°, 0.0°)$ from Ebisawa et al. (2005).

The radial distribution is generated from the sources with $S > 1.5 \times 10^{-14}$ erg s^{-1} cm^{-2}, plotted over the stellar distribution models (green shade) and the $1/\theta$ distribution (blue dashed). The result under the PL+Fe model (black solid) shows slightly higher concentration than the PL model (red dotted). Both the stellar and $1/\theta$ distributions are averaged over the ACIS-I FoV ($16' \times 16'$) of the GB fields.

The stellar distribution is derived from the Galactic stellar model, which consists of the central spherical cluster, the central disk, the triaxial ellipsoidal GB and the Galactic disk (Muno et al. 2006, hereafter M06; Launhardt et al. 2002, hereafter L02; Kent et al. 1991 hereafter K91). For the first three components, we use the formula and the parameter values in L02 and M06. For the Galactic disk, M06 uses a simple exponential form from K91 and for the overall normalization, M06 uses 10^{11} $M_\odot$, but since the first three components are mainly for the stellar mass, we use the normalization to match the local stellar mass density of 0.044 $M_\odot$ ps^{-3} (Robin et al. 2003). This gives 1.8×10^{10} $M_\odot$ for the whole disk, which is close to 2.2×10^{10} $M_\odot$ in (Robin et al. 2003). The model has about a factor of two uncertainty (M06, L02) and for comparison, we show two cases of the integration along the line of the sight: 6 to 10 kpc (solid green, M06) and 6 to 8 kpc (dashed-dot green) to explore the possible depth coverage of X-ray sources.

The relative normalization of the stellar and $1/\theta$ distributions is set by a simple χ^2 fit to the result under the PL+Fe model. The difference in the shape of the radial distribution of the stellar model between two depth coverages is minimal due to the near symmetry of the model with respect to the GC and the high concentration around the GC, but the relative normalization to the X-ray source density between two is different, proportionally to the assumed volume coverage.

The radial distribution shows the GB X-ray sources are highly concentrated at the GC, more heavily than the stellar models. It also shows the GB X-ray sources extend out to > 1.5 ° from the GC, following roughly the $1/\theta$ relation with some excess in Arches Cluster, Sgr C and Sgr B fields. The above results indicate 0.60 ± 0.18 X-ray sources arcmin^{-2} at $S > 1.5 \times 10^{-14}$ egs cm^{-2} s^{-1} in the Sgr A* field from the 100 ksec observation under the PL+Fe model (0.86 ± 0.26 arcmin^{-2} from the stacked results; the error is derived from the 25% systematic errors of the model choice). This is consistent with 0.61 ± 0.13 X-ray sources arcmin^{-2} from M03, which assumes a power law spectrum with Γ = 0.5, $N_{\rm H} = 6 \times 10^{22}$ cm^{-2} and the GC at 8 kpc.

5. DISCUSSION

The large extent of the $1/\theta$ relation in the radial distribution and the similarly hard spectral type of the X-ray sources found in the windows fields and the other GB fields indicate the observed GB X-ray sources within at least $\sim$ 200 pc from the GC may consist of the similar population of X-ray sources in the same central cluster.

5.1. *GB X-ray Source Population*

Recent population synthesis models by Ruiter et al. (2006) show IP can constitute the majority of the GB X-ray sources, while Liu & Li (2006) draw a different conclusion from their model. The main difference comes from the mass transfer rate in IPs, which makes the luminosity estimates of IPs by Liu & Li (2006) ($\lesssim 10^{31}$ erg s^{-1}) substantially lower than the same by Ruiter et al. (2006) ($\sim 10^{30-32}$ erg s^{-1}).

van den Berg et al. (2008) finds 4 CV candiates in the HST observation of the LW field, which appear to be non-local ($\gtrsim 2-3$ kpc) and the X-ray properties of the two are consistent with IPs. Koenig et al. (2007) reported 3 CVs in the 5 GB *Chandra*/ACIS fields, and van den Berg et al. (2006b) reported 5 CV candidates in each of the BW and LW fields. These results contrast with Grindlay et al. (2005), who did not find any CV candidate in the 15 *Chandra* anti-GC fields. These results also imply the increasing gradient of the CV density toward the GC. Note the CVs in Koenig et al. (2007) are likely within 3 kpc.

Assuming the majority of the detected GB X-ray sources are CVs, we derive the CV density relative to the stellar density. Table 4 summarizes the number density of X-ray sources with $S/N > 3$ in the H_C band in the GB fields and compare them with the stellar density of two different models. If we assume the X-ray sources follow the stellar density, we can further assume the majority ($> 85\%$) of the detected X-rays are at a 6 – 10 kpc distance, considering the stellar distribution peaking at the GC. The table compares the average density over the volume set by 6 – 10 kpc distance in the $16' \times 16'$ FoV.

The first stellar model (A) is the same stellar mass model used in Fig. 5 (M06, L02, K91). We use a local value of 0.144 stars pc^{-3} and 0.044 $M_\odot$ pc^{-3} to convert the mass density to the number density (Picaud & Robin 2004; Robin et al. 2003). For comparison, we also use another stellar model (B) by Picaud & Robin (2004) which consists of the Galactic disk and Bulge. This model is designed to describe the stellar density at the outer Galactic Bulge. This model is properly normalized at the local Galaxy (0.145 star pc^{-3}), but due to the lack of the Galactic nucleus component, the stellar density for the GB fields within 1° offset from the GC is underestimated. Two models agrees within $< 30\%$ at the windows fields where Galactic Nucleus components are not important.

In the following, we assume the model (A) for tracing the X-ray density seen in the GB fields. The model (A) predicts $\sim 1 - 5 \times 10^{-7}$ X-ray to stellar density and since we expect about 1% of CVs being detected in the X-ray data (M06), this result is consistent with the local CV to stellar density of 7×10^{-5} and thus the majority of the detected X-ray source being CVs. Since all the known IPs are about 5% of all the known local CVs, this result is consistent with the majority of X-ray sources being IPs.

However, it may be too early to rule out other classes of sources such as polars that may have a significant contribution. The fraction of the known polars among the known CVs is about 20%. Ramsay & Cropper (2004) founds X-ray selected polars, traditionally known soft, are not so soft as considered, and some polars also show He-like Fe-line emission. Therefore, some of the GB hard sources considered as IPs in fact can be polars. In addition to CVs, Sakano et al. (2005) reported unusual transients in the Sgr A* field and Chaty (2008) discovered the new class of heavily obscured HMXBs. Since these sources can hide their companion with its interal absorption, they may not be easy to identify even with deep IR imaging.

As shown in this paper, the X-ray variability may also change the apparent source distribution, so that in order to understand the true distribution, continuous monitoring of the GB fields and the full analysis of the long term data are necessary. Considering the X-ray variability of sources, the true distribution of the GB X-ray population in the GB fields of 100 ksec can be at least 30-40% higher than what has been observered so far.

TABLE 4
X-RAY SOURCE AND STELLAR (MASS) DENSITY FOR 6–10 KPC[a]

Field	X-ray sources[b]	Stellar model (A)[c]		Stellar model (B)[d]	
	10^{-7} pc^{-3}	Stars pc^{-3}	X-ray to stars 10^{-7}	Stars pc^{-3}	X-ray to stars 10^{-7}
BW	3.2	2.1	1.6	3.2	1.0
SW	4.9	5.3	0.9	6.7	0.7
LW	24 – 26	7.6	3.2 – 3.4	8.3	2.9 – 3.1
Srg B2	55 – 68	42	1.3 – 1.6	8.8	6.3 – 7.8
Srg C	100 – 110	46	2.2 – 2.4	8.9	11 – 12
Arches	180 – 200	53	3.4 – 3.8	9.1	19 – 22
Sgr A*	230 – 380[d]	70	3.2 – 5.5	9.1	26 – 42

(a) Assumes the detected hard X-ray sources or stars seen within the $16' \times 16'$ FoV are mainly (more than 90%) from the 6–10 kpc distance. (b) The range is set by two model classes (PL and PL+Fe). (c) The composite model in M06 and the references therein. The model gives the stellar mass density in the unit of $M_\odot$ pc^{-3}, and we assume the local value of 0.144 stars pc^{-3} and 0.04 $M_\odot$ pc^{-3} to get the star number density (Robin et al. 2003). This relation should be good for the bulge in the case of CVs and ABs, but perhaps not good for YS (Sazonov et al. 2006). (d) Stellar density model by (Picaud & Robin 2004) for the outer Galalctic Bulge. The model consists of the Galactic disk and Galactic Bulge, but no nucleus. See §5.2. (e) The range is set by the 100 ksec observation under PL and the stacked data under PL+Fe.

While the optical/IR observations provide some clue on the population, the true nature may not be resolved due to source crowding in the case of windows fields and the heavy extinction in the other GB fields on the plane. A scheduled deep observation ($\sim$ 1 Msec) on the LW, designed to investigate the exact nature of the GRXE in the field, will provide an opportunity of studying the nature of the X-ray point sources in the LW in relation with the X-ray sources found in the Sgr A* field. For instance, such a deep observation will allow the direct detection of the iron line in some of the sources. As the time of writing this paper, more than 1 Msec of the Sgr A* field are compiled and an initial analysis on the stacked data in the limited 4–8 keV band has been presented by Revnivtsev & Sazonov (2007), but the detailed analysis of the variability of X-ray sources and sources with Fe-line emission may give hints on the relative population of the IPs and the rest of source types.

5.2. *X-ray Diffuse Emission and X-ray Point Source Surface Luminosity*

The nature of the GRXE has been debated since its discovery. With excellent angular resolution of *Chandra*, it is hopeful that one can resolve all the X-ray point sources, and thus answering the question of whether or not there is a diffuse component in the GRXE, but the debate is still not over.

The analysis on the 100 ksec *Chandra* observation of two Galactic plane fields around $(l,b) \sim (28.5°, 0.0°)$ illustrates the disagreement in the community. Ebisawa et al. (2005) argued the X-ray point sources explain at most 10% of the GRXE and that no known class of possibly unresolved sources can make up the deficit and thus they claimed a truly diffuse component should be present in the GRXE. However, Revnivtsev & Sazonov (2007), using the same data and the X-ray luminosity function in the local Galaxy by Sazonov et al. (2006), claimed the GRXE can be explained by the X-ray point sources including the unresolved point sources. The similar morphology of the GRXE and IR surface brightness tracing the stellar distribution supports their argument indirectly. The origin of the diffuse hard X-ray emission remains theoretically challenging as well since it is difficult to gravitationally confine the thermally hot ($\gtrsim$ 5 keV) plasma and the alternative non-thermal models do not satisfy the observed data completely (Muno et al. 2004a)

Fig. 4 shows our X-ray point source distributions in the GB fields fall short of the required source distribution to explain the GRXE (see also Fig. 9 in Ebisawa et al. (2005)). The GRXE is calculated for 2–10 keV band, and the overall flux contribution of 8–10 keV is $\lesssim$ 20–30% (see Fig. 8 in Ebisawa et al. (2005)). Note although we are comparing the different region of the Galactic plane, the GB fields here are expected to have more X-ray point sources than the field analyzed by Ebisawa et al. (2005) due to the proximity of the GC. Therefore, our results support the idea of the presence of a truely diffuse component.

The following paper (Hong et al. 2008) will address the (unresolved) diffuse emission in the GB fields including the regions covered by our Bulge latitude survey (over $1^\circ \times 2^\circ$), but here we compare the X-ray surface luminosity from the X-ray point sources to explore the origin of the discrepancy in the interpretation of the GRXE.

Table 5 summarizes the specific luminosity estimates of the various studies in the *Chandra*/ACIS energy range. From comparing the results under PL+Fe with the stellar model we expect $0.9-2.1\times10^{-6}$ X-ray sources $M_\odot{}^{-1}$ at $S > 1.5\times10^{-14}$ erg s^{-1} cm^{-2} (1.1×10^{32} erg s^{-1} for sources at the GC). The range covers the two different model depth ($6-8$ vs. $6-10$ kpc) and two results for the Sgr A* field (100 vs. 750 ksec). Using Eq. 7 in M06, we get $1.6-3.7\times10^{26}$ erg s^{-1} $M_\odot$ in $2-8$ keV from $5\times10^{32}-10^{34}$ erg s^{-1}. M06 got $5\pm2\times10^{26}$ erg s^{-1} $M_\odot{}^{-2}$ in $0.5-8$ keV from the X-ray sources in the GB X-ray sources. M06 also interpreted the result of Sazonov et al. (2006) to be $1\pm0.3\times10^{27}$ erg s^{-1} $M_\odot$ in $2-10$ keV for the local Galaxy. From a similar scaling, the X-ray emissivity of $7.7\pm3.9\times10^{27}$ erg s^{-1} $M_\odot{}^{-1}$ in 2–10 keV from the Sgr A* field by Revnivtsev et al (2007) becomes $2.6\pm1.3\times10^{27}$ erg s^{-1} $M_\odot{}^{-1}$ for $5\times10^{32}-10^{34}$ erg s^{-1} in 2–10 keV. MO6 claimed their result is consistent with Sazonov et al. (2006), but in the same $2-10$ keV band, the surface flux in M06 is 4.1×10^{26} erg s^{-1} $M_\odot{}^{-1}$ and for $2-8$ keV band, the results in M06 becomes 3.3×10^{26} erg s^{-1} $M_\odot{}^{-1}$ under $\Gamma = 1.5$ and $N_{\rm H} = 6\times10^{22}$ cm^{-2} used in their paper, so that there is a hint of mismatch between the two. This also makes M06's results more consistent with ours. Note under the same depth coverage (6–10 kpc), our result gives 1.6–1.8 $\times$ 10^{26} erg s^{-1} $M_\odot{}^{-1}$.

It is hard to compare these flux values fairly due to many different underlining assumptions in the calculation. In our analysis, the mismatch in the spatial distribution between in the stellar model and the X-ray distribution (Fig. 5) makes the relatively normalization between the X-ray and stellar sources somewhat arbitary. In the case of the Sgr B2 field, M06 shows a factor of three or four lower source density compared the other GB fields in the same offset from GC. So the narrow FoV coverage here may have contributed the discrepancy between the stellar model and X-ray distributions. For instance, if we fit the relative normalization of the stellar distribution with the X-ray distribution within 1° from the GC such as the Sgr A*, Arches, and Sgr C, we get about a factor of 2 higher normalization value and the specific luminosity of the X-ray point sources.

Even with these uncertainties, there seems to be noticeable difference among these results and our finding on the surface luminosity of resolved X-ray point sources in the GB fields. Therefore the interpretations of the GRXE vary as well. In fact, the contribution of the resolved X-ray point sources to the GRXE differs a factor of 2 or more among the groups; at $(l,b)\sim(28.5^\circ,0.0^\circ)$ Ebisawa et al. (2005) estimated it to be about 10% in the 2–10 keV band while Revnivtsev & Sazonov (2007) reported 25% in the 1–7 keV band from the same data and also $\sim$ 25% in the Sgr A* field in the 4–8 keV band.

Now the question of the diffuse component in the GRXE comes down to whether the remaining seemingly-diffuse emission can be explained by the unresolved faint point sources, so perhaps the clear agreement on the luminosity function of the resolved X-ray point sources may have to proceed before understanding the nature of the unresolved emission.

As the careful selection of spectral model and its parameters as well as the energy range is important, the different choices among groups perhaps explains the different outcomes. As illustrated in Fig. 4, the $1-7$ keV band used in Revnivtsev & Sazonov (2007) can be still susceptible to generate the noticable uncertainties arising from the choice of the spectral models due to inclusion of the soft energy range 1-2 keV. In the case of Revnivtsev et al (2007), the 4–8 keV energy range is used to drive the specific luminosity of the X-ray sources in the Sgr A* field. Since the 4–8 keV band is less susceptible to the variation of the interstellar absorption in the given range ($\sim 6\times10^{22}$ cm^{-2}), and the majority of the sources are expected to be near the GC, so the flux values seem to be well defined, but the narrow band choice makes it hard to determine the proper spectral model and its parameters and the actual decoupling of the spectra between the resolved point sources and unresolved point sources has not attempted in the paper.

6. CONCULSION

In the log$N$-log$S$ distribution of the sources in the GB fields, the systematic errors arising from incorrect assumption of spectral type is usually disregarded due to lack of alternative approaches, but they often dominate other systematic errors such as EB, completeness or even statistical errors. The quantile analysis allows a robust method to assign a proper spectral type for flux calculation. The technique is shown reliable in the hard band (> 2 keV), insensitive to selection of the spectral model classes. In the soft band (< 2 keV), where the Galactic extinction has a great influence in the spectra, the result can vary drastically depending on the assumed spectral model class. Therefore, the result in the soft band should be taken with caution.

The log$N$-log$S$ and radial distribution of the GB fields including the three low extinction windows show the high concentration of the X-ray sources in the GB. The GB distribution clearly extends out to $\sim 1.5^\circ$ (LW) from the center and possibly more. The spectral type of the GB X-ray sources appears to be largely consistent across the region with the iron line, and it is possible that one type of sources constitute the majority of the GB population, and the estimated X-ray density is consistent with the majority being CVs, but the relative contribution of IPs and other types are uncertain. Our results require truly diffuse X-ray components to explain the GRXE. The disagreement among the groups on the nature of the GRXE originates at least partially from the disparity on the overall luminosity of the resolved X-ray point sources.

This work is supported in part by NASA/Chandra grants

TABLE 5
SPECIFIC LUMINOSITY OF X-RAY POINT SOURCES

Source	Reported (10^{26} erg s^{-1} $M_\odot$ $^{-1}$)	Energy Range (keV)	Luminosity Range (erg s^{-1})	Field	Scaled 2 – 8 keV for $10^{32.7-34}$ erg s^{-1} (10^{26} erg s^{-1} $M_\odot$ $^{-1}$)
This Study	1.6 – 3.7	2–8	$10^{32.7-34}$	7 GB fields (100, 750 ksec)	1.6 – 3.7
M06	5.0 ± 2	0.5–8	$10^{32.7-34}$	3 GB fields and shallow GC Strip	3.3 ± 1.3
Sazonov et al. (2006)	45 ± 9	2–10	10^{27-34}	the local Galaxy	9 ± 3
Revnivtsev et al (2007)	77 ± 39	2–10	10^{30-33}	the Sgr A* field (1 Msec)	26 ± 13

AR1-2001X, AR2-3002A, AR3-4002A, AR4-5003A and NSF grant AST-0098683.

REFERENCES

Bogdanov,S., Grindlay, J. E., & van den Berg, M., 2005 ApJ, 630, 1029.
Cappelluti, N. et al. 2005, ApJ, 430, 39.
Chaty, S., 2008 astro-ph/0805.1486
Drimmel, R., Cabrera-Lavers, A., & Lopez-Corredoira, M., 2003, ApJ, 409, 205.
Ebisawa, K., et al. 2005, ApJ, 635, 214.
Freeman, P.E. et al. 2002, ApJS, 138, 185.
Gehrels, N. et al. 1986, ApJ, 303, 336.
Grindlay, J.E. et al. 2005, ApJ, 635, 907
Hong, J, Schlegel, E. M. & Grindlay, J. E., 2004, ApJ, 614, 508. (H04)
Hong, J, et al. 2005, ApJ, 635, 907. (H05)
Hong, J, et al. 2008, in preparation
Koenig, X. et al. 2007, ApJ, in pulication
Kim, E. et al. 2007, ApJ, 659, 29
Kent, S. M., Dame, T. M., & Fazio, G. 1991, ApJ, 378, 131
Launhardt, R., Zylka, R., & Mezger. P. G. 2002, A&A, 384, 112
Laycock, S. et al. 2005, ApJL, 634, 53 (L05)
Liu, X. W. & Li, X. D. 2006 AA, 449, 135.
Muno, M. P. et al. 2003, ApJ, 589, 225 (M03)
Muno, M. P. et al. 2004, ApJ, 613, 326
Muno, M. P. et al. 2004, ApJ, 613, 1179 (M04)
Muno, M. P. et al. 2006, ApJS, 165, 173 (M06)
Picaud, S. &, Robin. A. C. 2004, A&A, 417, 651
Ramsay, M. & Cropper, M. 2004, MNRAS, 347, 497.
Ruiter, A., Belczynski, K. & Harrison, T. 2006, ApJL, 640, 167.
Revnivtsev, M. & Sazonov, S., 2007 A&A, 471, 159.
Revnivtsev, M., Vikhlinin, A. & Sazonov, S., 2007 A&A, 473, 857.
Robin, A. C. et al., 2003, A&A, 409, 523.
Sakano, M. et al. 2005, MNRAS, 357, 1211.
Sazonov, S. et al. 2006, A&A, 450, 117.
Schlegel, D., Finkbeiner, D. & Davis, M., 1998, ApJ, 500, 525.
Stanek, K. Z. 1998, Astro-ph/9802307
van den Berg, M. et al. 2006a, ApJL, 135, 647
van den Berg, M. et al. 2006b, HEAD meeting, 9, 1.44
van den Berg, M. et al. 2008, ApJ submitted
Wang, Q. D. , Gotthelf, E. V. & Lang, C. C., 2002, Nature, 415, 148.
Wijnands, R., et al. 2005, ApJ, 618, 883